

A Neuromorphic Architecture for Reinforcement Learning from Real-Valued Observations

Sérgio F. Chevtchenko^{a,*}, Yeshwanth Bethi^b, Teresa B. Ludermir^a, Saeed Afshar^b

^a*Centro de Informática - CIn, Universidade Federal de Pernambuco, Av. Jornalista Aníbal Fernandes, s/n, Cidade Universitária, 50.740-560, Brazil*

^b*International Centre for Neuromorphic Engineering, MARCS Institute, Western Sydney University, Werrington, NSW 2747, Australia*

Abstract

Reinforcement Learning (RL) provides a powerful framework for decision-making in complex environments. However, implementing RL in hardware-efficient and bio-inspired ways remains a challenge. This paper presents a novel Spiking Neural Network (SNN) architecture for solving RL problems with real-valued observations. The proposed model incorporates multi-layered event-based clustering, with the addition of Temporal Difference (TD)-error modulation and eligibility traces, building upon prior work. An ablation study confirms the significant impact of these components on the proposed model's performance. A tabular actor-critic algorithm with eligibility traces and a state-of-the-art Proximal Policy Optimization (PPO) algorithm are used as benchmarks. Our network consistently outperforms the tabular approach and successfully discovers stable control policies on classic RL environments: mountain car, cart-pole, and acrobot. The proposed model offers an appealing trade-off in terms of computational and hardware implementation requirements. The model does not require an external memory buffer nor a global error gradient computation, and synaptic updates occur online, driven by local learning rules and a broadcasted TD-error signal. Thus, this work contributes to the development of more hardware-efficient RL solutions.

Keywords: spiking neural networks, FEAST, STDP, reinforcement learning.

*Corresponding author

Email addresses: `sfc@cin.ufpe.br` (Sérgio F. Chevtchenko),
`y.bethi@westernsydney.edu.au` (Yeshwanth Bethi), `tbl@cin.ufpe.br` (Teresa B. Ludermir), `S.Afshar@westernsydney.edu.au` (Saeed Afshar)

1. Introduction

Reinforcement Learning (RL) is a bio-inspired paradigm within machine learning, where an agent learns to make decisions by interacting with an environment and receiving feedback in the form of rewards (Sutton & Barto, 2018). It has been successfully used in various domains, ranging from game-playing AI (Mnih et al., 2015) to self-driving cars, robotics (Hwangbo et al., 2019), and much more. In recent years, deep reinforcement learning (DRL) has emerged as a promising approach, combining RL with the scalability and representation power of deep neural networks (DNNs). However, despite these advancements, the computational efficiency of deep neural networks still remains a challenge. Training DRL systems often require thousands of hours of training on energy-intensive computational resources like GPUs and TPUs.

An alternative approach is offered by biologically inspired, spiking or event-based, neural networks. These networks aim at emulating the computational principles found in biological brains, such as the propagation of information through discrete spikes, spatio-temporal processing and local learning rules. Although bio-inspired methods have the potential to mitigate some of the challenges encountered by DNNs—particularly in the area of power efficiency and online learning—the use of SNNs for complex RL problems is still an area of active research (Akl et al., 2023).

In this paper, we introduce a novel neuromorphic architecture designed to tackle reinforcement learning problems with real-valued observations. Drawing inspiration from prior works (), our network incorporates event-based clustering and introduces modulation by a global signal through eligibility traces. The effectiveness of the proposed model is assessed against a tabular actor-critic algorithm with eligibility traces and a state-of-the-art DRL model, Proximal Policy Optimization (PPO). The results demonstrate that our network provides an appealing trade-off in terms of computational and hardware implementation requirements when compared to PPO on three classic RL control tasks.

This paper is structured as follows. A review of related literature and comparison to the present work is provided in Section 2. The proposed model is described in Section 3 and is experimentally compared to baseline models in Section 4. Concluding remarks and discussion of possible future endeavors can be found in Section 5.

35 2. Related works

36 Deep learning has shown impressive results in the domain of Reinforcement
37 Learning and has surpassed all other conventional methods to be the state-of-
38 the-art architectures for training autonomous agents particularly on sparse re-
39 ward structures. However, the training procedures for Artificial Neural Net-
40 works (ANNs) have always been resource-intensive in terms of computation and
41 memory requirements. Deploying ANNs at the edge with low-power constraints
42 and training them online still remains a challenge due to the same reason. Re-
43 cent advances in neuromorphic computing and training Spiking Neural Network
44 (SNN) architectures offer novel solutions to building low-power machine intel-
45 ligence. SNN architectures that use binary valued spikes (or events) for both
46 computation and communication provide excellent energy efficiency benefits.
47 With the uptake in the adoption of neuromorphic sensors like DVS (Lichtsteiner
48 et al., 2008) and ATIS (Posch et al., 2010), event-driven machine learning algo-
49 rithms are also being explored for low-latency and low-power applications of
50 neuromorphic computing (Gallego et al., 2020).

51 Training SNN architectures is still an active area of research, and many at-
52 tempts have been made to approximate the error backpropagation and gradient
53 descent techniques used to train ANNs and train SNNs. For example, Bellec et al.
54 (2020) proposed a spiking neural network learning rule called e-prop that can be
55 applied to recurrent spiking networks. This rule is shown to approximate the
56 performance of an LSTM network, trained via backpropagation through time on
57 two discrete Atari games. Other methods use surrogate gradients with stand-
58 in differentiable alternatives for non-differentiable parts of SNN architectures
59 (Neftci et al., 2019). For instance, Akl et al. (2023) propose a combination of
60 DRL frameworks with a spiking architecture through the use of surrogate gradi-
61 ents and the backpropagation through time (BPTT) algorithm. However, these
62 methods also face the same problem of requiring energy-intensive computational
63 resources to perform the error backpropagation. The error back-propagation ap-
64 proximations are also not bio-plausible as they would require symmetric back-
65 ward pathways that transfer precise continuous-valued gradients and, in some
66 cases, non-causal operations like Back-Propagation Through Time (BPTT). Bio-
67 plausible local learning rules that can train individual nodes in SNN architectures
68 using only information available at each neuron, can offer a solution to this prob-
69 lem. Spike-Timing-Dependent Plasticity (STDP) has been the most commonly
70 used local learning rule for SNN architectures to perform unsupervised learning.
71 STDP can train spiking neurons to learn the spatio-temporal features that reflect

72 the statistics of the input spiking data. The Hebbian learning rule has primar-
73 ily been used in unsupervised learning settings to learn some useful features for
74 tasks like pattern classification (Diehl & Cook, 2015). However, unsupervised
75 learning rules like STDP neglect any information related to the “success”, “fail-
76 ure”, or “novelty” of the inputs and outputs (Frémaux & Gerstner, 2016).

77 R-STDP (Reward-modulated Spike Timing-Dependent Plasticity) is a Spiking
78 Neural Network (SNN) learning rule that governs the changes in the strength of
79 connections between neurons such that the plasticity of synapses is modulated
80 by reward signals that reinforce or weaken the connections between neurons
81 based on the timing of their spikes. Izhikevich (2007), Florian (2007) and Leg-
82 enstein et al. (2008) independently laid the groundwork for R-STDP modulated
83 spiking networks. In order to demonstrate the computational and temporal ca-
84 pabilities of this approach, a fully connected multilayered network of spiking
85 neurons is shown by Florian (2007) to solve a temporally coded XOR problem
86 with a delayed reward. Vasilaki et al. (2009) used a reward-modulated STDP
87 learning rule on the action layer in combination with an input place cell layer to
88 perform reinforcement learning on a Morris water maze puzzle. While theoreti-
89 cal models have used reward-modulated STDP for over a decade, recent research
90 has provided experimental evidence of the role of eligibility traces in Reinforce-
91 ment Learning (RL)(Gerstner et al., 2018). The R-STDP rule used in the present
92 work is a simplified version of RMSTDPET found in the work by Florian (2007).
93 Actor-critic models with temporal difference (TD) are proposed by Potjans et al.
94 (2011), and later Frémaux et al. (2013). A more general three-factor learning rule
95 is later introduced by Frémaux and Gerstner (2016).

96 A key component of reinforcement learning is the development of useful in-
97 ternal representations of complex environments to evaluate and utilize the cur-
98 rent state of the environment. This allows the system to decide on actions that
99 provide maximum future rewards (Sutton & Barto, 2018). Various internal rep-
100 resentations for inputs have been used by the SNN solutions for reinforcement
101 learning. One strategy is to use manually selected partitions of the input space
102 to generate spiking inputs for various states. Potjans et al. (2009) and Jitsev et al.
103 (2012) used a fixed cluster of neurons that represent the state space and individu-
104 ally fire for each particular state. Frémaux et al. (2013) used pre-determined place
105 cells to act as input to their continuous time spiking actor-critic architecture.
106 Friedrich et al. (2014) used population coding for the input layer representation.
107 These methods manually partition the input space or use a population that uni-
108 formly covers the entire input space of any given environment. A drawback of
109 these early models is that the implemented networks fully encode the observed

110 state in the input layer, functionally similar to classical tabular RL algorithms.
111 In other words, each neuron in the input layer is used to encode a specific state
112 of the environment. Also, this approach does not scale well with increasing in-
113 put dimension. This limitation in scalability is addressed in our previous paper
114 (Chevtchenko & Ludermir, 2020) by a four-layered network with a hidden layer
115 inspired by place cells. However, this approach often requires a large number of
116 place neurons and relies on discrete and finite observations.

117 Other approaches to represent the input space include using the reservoir
118 computing paradigm (Schrauwen et al. (2007);Lukoševičius and Jaeger (2009)).
119 Reservoir computing involves projecting the low dimensional inputs to a high
120 dimensional representational space by using a population of recurrently con-
121 nected neurons such that states not linearly separable in the input space can be
122 separated in the representational space (Maass et al., 2002). Weidel et al. (2021)
123 used reservoir computing with unsupervised plasticity on the inputs and apply
124 reward modulated learning on the output layer that generated actions. However,
125 most of these SNN architectures predominantly use rate coding, which does not
126 offer the same level of energy efficiency that sparse temporal coding provides.

127 Another promising approach towards realizing low-power spike-based learn-
128 ing algorithms lies in the employment of event-driven neuromorphic algorithms.
129 These are principally aimed at hardware deployment and aim for improved scal-
130 ability through collocation of processing and memory, as well as facilitating low-
131 latency computation (Schuman et al., 2022).Neuromorphic event-driven algo-
132 rithms emulate spiking neuron architectures that are tailored for computational
133 efficiency and performance. HFirst algorithm (Orchard et al., 2015) is an exam-
134 ple of a multi-layered network architecture that is based on the HMAX algorithm
135 (Serre et al., 2007) which itself inspired by visual cortex to learn features from
136 event-based data using an event-driven approach of processing data. The Hier-
137 archy of Event-based Time Surfaces (HOTS) (Lagorce et al., 2016) is another un-
138 supervised multi-layered feature extraction algorithm that uses the same neuron
139 update rule based on the cosine distance of weights to the input representation
140 introduced in Ballard and Jehee (2012) to model sensory features in cortical neu-
141 rons. The HOTS algorithm uses multiple layers to extract spatio-temporal pat-
142 terns at multiple hierarchical levels with different time constants by performing
143 clustering. Afshar et al. (2020) introduced an unsupervised feature extraction al-
144 gorithm called Feature Extraction using Adaptive Selection Thresholds (FEAST),
145 which is also capable of learning hierarchical spatio-temporal features by using
146 adaptive thresholds for each neuron to promote equal activation of neurons.

147 The majority of the neuromorphic feature extraction algorithms are primarily

148 targeted toward performing tasks on event-based data. The FEAST method has
 149 been used for a range of applications such as event-based object tracking Ralph
 150 et al. (2022), activity-driven adaptation in SNNs Haessig et al. (2020), and spoken
 151 digits recognition task Xu et al. (2022). Recently a generalization of the FEAST
 152 algorithm has been proposed in Bethi et al. (2022) to perform supervised learn-
 153 ing on spiking data using reward and punishment of neurons through threshold
 154 adaptation. We can utilize the same neuromorphic principles and apply these
 155 architectures to the reinforcement learning domain to partition the input state
 156 space that can dynamically adapt to the reward structure and performance of
 157 the agent. In this work, we modify the neuron layers proposed in the Bethi et al.
 158 (2022) to simultaneously perform unsupervised clustering of the input space and
 159 modulate it based on the ongoing TD-error of an actor-critic agent that utilizes
 160 the learned representation. We show that partitioning achieved by the neurons
 161 represents different parts of the input space with varying degrees of density and
 162 resolution depending on the ongoing performance of the actor-critic agent using
 163 the representation. We demonstrate the quality of the input space representa-
 164 tions by using a conventional tabular actor-critic algorithm and applying it to
 165 various environments.

166 3. The proposed architecture

167 The proposed network has two main components: i) an initial clustering
 168 layer(s) for dimensionality reduction and partitioning of the input space and ii)
 169 actor-critic neurons for learning from the previously reduced state-space repre-
 170 sentation. The following sections provide a detailed description of each layer
 171 and corresponding plasticity rules.

172 3.1. Input layer

173 The input signal is represented by a vector of real-valued observations $\vec{x} =$
 174 $[x_1, x_2, \dots, x_n]$. These are provided by the environment in discrete time-steps at
 175 time t , along with the reward signal $r(t)$. Considering N_i neurons in the input
 176 layer, each neuron can be fully connected to the input signal through an array
 177 of synaptic weights, as illustrated in Figure 1. Euclidean distance is used as a
 178 metric to find the closest neuron i with weights \vec{w}_i matching the input context
 179 \vec{x} . Each neuron i also contains a scalar threshold parameter θ_i that is used for
 180 the selection of the closest neuron. The value v_i of a neuron in the input layer is
 181 calculated as the Euclidean distance between input and weight vectors:

$$v_i(t) = \|\vec{w}_i(t) - \vec{x}(t)\|, \quad (1)$$

182 where $v_i(t)$ is the value of the neuron i at time t , \vec{w}_i are the weights connect-
 183 ing the neuron i to the input vector \vec{x} . The value v_i of every neuron is compared
 184 to its corresponding threshold value θ_i to check if the neuron is eligible to be
 185 activated. A winner-take-all (WTA) activation is adopted for an entire layer or
 186 a group of neurons within the same layer. The winning neuron should have the
 187 least value among the neurons with values within their corresponding thresh-
 188 olds. This rule ensures that only the neuron with the least euclidean distance
 189 within the eligible neurons will produce a spike for the next layer. Additionally,
 190 if no neuron is eligible through the above rule, WTA activation elects the neuron
 191 with the lowest value, regardless of the corresponding threshold.

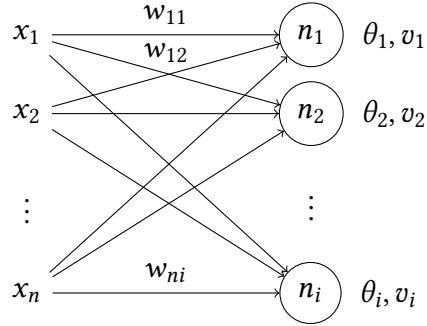


Figure 1: Illustration of the input layer of the proposed model.

192 Neurons in this layer are subject to weight and threshold plasticity, with the
 193 aim of providing a compact representation of the input space. This plasticity
 194 has two drivers: i) adaptation to the input signal and ii) modulation by the feed-
 195 back from the actor-critic layer. The first adaptation rule is based on Feature
 196 Extraction with Adaptive Selection Thresholds (FEAST), proposed by Afshar et
 197 al. (2020).

198 In order to illustrate this adaptation rule, consider a two-dimensional input
 199 vector $\vec{x} = [x_1, x_2]$, as illustrated in Figure 2. The input signal \vec{x} and the weights
 200 of two input neurons are represented by two-dimensional vectors. The threshold
 201 of each neuron is a scalar and represents the receptive field of a neuron in the
 202 shape of a circle around the weight vector.

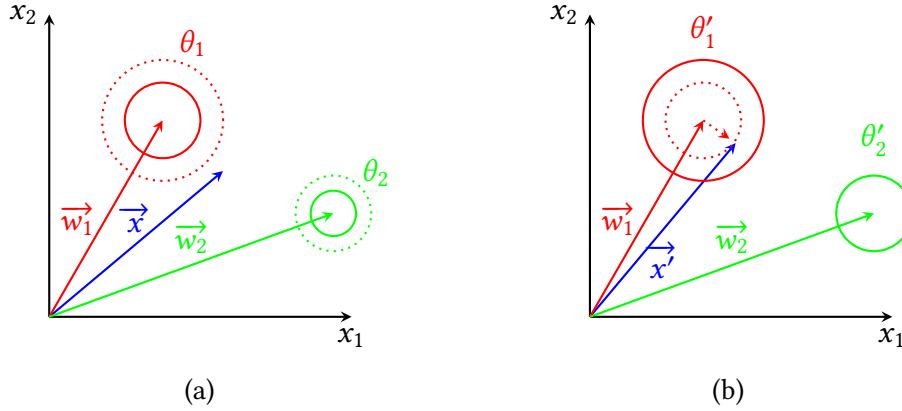


Figure 2: An illustration of synaptic plasticity rule based on FEAST (Afshar et al., 2020) using Euclidean distance. A two-dimensional input is considered. (a) The input vector \vec{x} is outside the threshold regions of both neurons. The neurons become more sensitive by increasing the thresholds. (b) A new input vector activates neuron 1. This results in adjustments of both the weights and the threshold of the active neuron.

203 An initial input signal \vec{x} , depicted in Figure 2a, falls outside the activation
 204 region of both neurons (solid circles). Thus, the value obtained by Equation 1
 205 is higher than θ_1 and θ_2 . When this occurs, all neurons in the layer have their
 206 thresholds increased by the parameter θ_{open} . This increases the receptive field
 207 size of each neuron in the layer, making it more likely for a neuron to be activated
 208 by an input signal.

209 On the other hand, Figure 2b illustrates the case of a new input vector \vec{x}'
 210 that activates the neuron 1. This is because the new value, i.e. the distance be-
 211 tween input and weight vectors, is within the threshold of the neuron. In order to
 212 increase the probability of activation of the same neuron in the future, when pre-
 213 sented with similar inputs, both threshold and weight are adjusted. The threshold
 214 is decreased and the weight vector moves in the direction of \vec{x}' , illustrated by the
 215 dotted circle and arrow in Figure 2b. As a result, the receptive field of the specific
 216 winning neuron contracts, reducing the chance of activation by distant inputs.
 217 The above adaptation, applied to activated neurons, is described by:

$$\Delta\theta_i = v_i(t) - \theta_i(t), \quad (2)$$

$$\Delta\vec{w}_i = \vec{x}(t) - \vec{w}_i(t), \quad (3)$$

$$\theta_i(t+1) = \theta_i(t) + \eta_{th} * \Delta\theta_i, \quad (4)$$

$$\vec{w}_i(t+1) = \vec{w}_i(t) + \eta * \Delta\vec{w}_i, \quad (5)$$

218 where $\Delta\theta_i$ and $\Delta\vec{w}_i$ are update values for the threshold and weights of neuron i
 219 and the respective update rates for each are η_{th} and η .

220 Figure 3 illustrates this adaptation process on a simulated dataset with three
 221 probability density functions (PDF). Three neurons are initialized with random
 222 weights and thresholds, as illustrated in Figure 3a. The weight of each neuron
 223 is depicted as a colored dot and the threshold region is delimited by same-colored
 224 arrows. The final configuration is depicted in Figure 3b, after 10^4 observations
 225 and using both η_{th} and η equal to 10^{-2} .

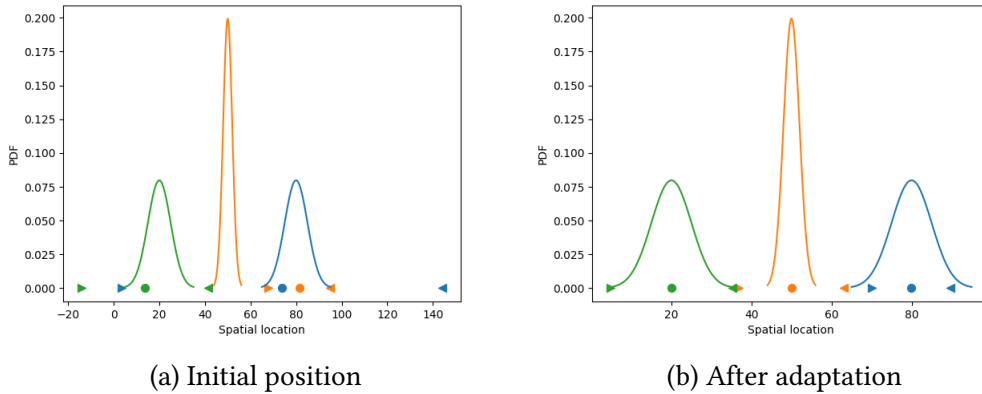


Figure 3: Clustering of neurons in the input layer on a simulated dataset with three Gaussian distributions and three input neurons. The weights of the three neurons are depicted by the colored dots and the corresponding thresholds are represented by the same-colored arrows.

226 Note that if more neurons are added to the clustering layer, the adaptation
 227 process described by Equations 2 to 5 will result in a denser, more granular repre-
 228 sentation of the observed state-space via neurons with smaller thresholds. This

229 is experimentally demonstrated in Figures 4a and 4b by using the same set of pa-
 230 rameters as in the previous experiments, but increasing the number of neurons
 231 from 3 to 10.

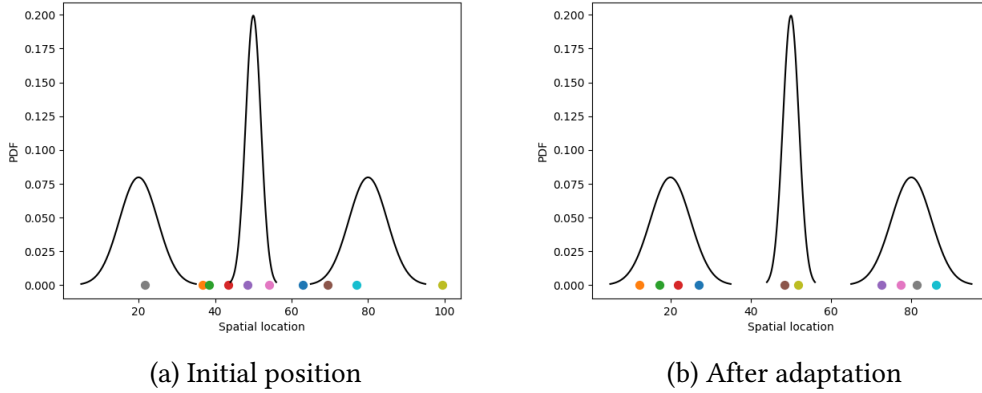


Figure 4: Clustering of neurons in the input layer on a simulated dataset with three Gaussian distributions and ten input neurons. Position of the colored dots on the X-axis represent the weights of the ten neurons used in the experiment. Thresholds are omitted for legibility.

232 In addition to the weight and threshold plasticity rule above, the proposed
 233 model implements modulation by feedback from the actor-critic layer. This is
 234 similar to the change in Equations 4 and 5, but η_{th} and η are scaled by temporal
 235 difference error δ and neural trace c_i . This modulation is described in more detail
 236 in Section 3.2.

237 The input layer neurons can encode the real-valued vector \vec{x} in a number of
 238 ways. In the present work we consider two possible configurations, as depicted in
 239 Figure 5: a) fully connected and b) individual encoding for each input dimension,
 240 followed by an additional clustering layer. Neurons grouped within a dotted
 241 rectangle represent a winner-take-all (WTA) activation mechanism, where the
 242 neuron possessing the highest potential transmits a pulse to the succeeding layer.

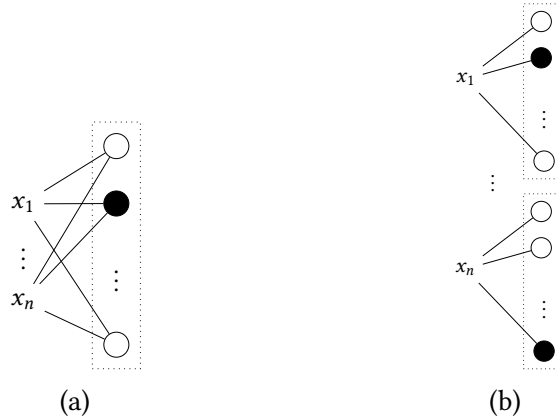


Figure 5: Diagrams of evaluated configurations for encoding the input vector by the first layer. (a) The input is fully connected to the neurons in the first layer with WTA activation. (b) A group of neurons is fully connected to a single input scalar and WTA is applied to each group separately.

243 Note that the configuration in Figure 5b produces multiple active neurons at
 244 each time-step, corresponding to the size of the input vector $\vec{x} = [x_1, x_2, \dots, x_n]$.
 245 In this case, a hidden clustering layer is used to provide a single winner neuron
 246 for the actor-critic layer, as illustrated in Figure 6. The WTA activation permits
 247 only one neuron from this second layer to generate a spike at any time step, thus
 248 explicitly enforcing sparsity at the layer level. The synapses between the first
 249 and second clustering layers are subject to the same modulation, as described
 250 by Equations 2 to 5, replacing the input vector \vec{x} by a larger multi-hot binary
 251 vector, representing activations in the previous layer.

252 3.2. Actor-critic layer

253 The actor-critic layer is a neuromorphic implementation of the tabular TD(λ)
 254 algorithm (Sutton, 1988). The actor is composed of N_a neurons, each representing
 255 a single discrete action. When a spike is produced by a single presynaptic neuron
 256 j , the resulting potential of an action neuron i is equal to the synaptic value w_{ij} .
 257 The action is then selected based on the highest potential, with the addition of
 258 random exploration:

$$a(t) = \begin{cases} \arg \max_i w_{i,j}, & \text{with probability } 1 - \epsilon \\ \text{random}, & \text{with probability } \epsilon, \end{cases} \quad (6)$$

259 where ϵ is the exploration probability. At the beginning of an episode ϵ is
 260 initialized at a maximum value 1 and is then gradually decreased to a small final
 261 value ϵ_{min} . The rate of decrease and the final baseline value are hyperparameters
 262 used to balance exploration and exploitation.

263 In the proposed system an action can be the result of a single or multiple
 264 neurons in the action layer spiking by using WTA activation. For instance, a
 265 movement in two dimensions can be encoded by two independent groups of
 266 neurons, each representing a one-dimensional action.

267 The value of a hidden state is represented by the weight connecting the value
 268 neuron to the hidden layer. Two separate synaptic eligibility traces are imple-
 269 mented for the actor and critic connections. These traces decay exponentially
 270 over time:

$$\vec{c}_c(t+1) = \vec{c}_c(t) - \frac{\vec{c}_c(t)}{\tau_c}, \quad (7)$$

$$\vec{c}_{ai}(t+1) = \vec{c}_{ai}(t) - \frac{\vec{c}_{ai}(t)}{\tau_a}, \quad (8)$$

271 where τ_a and τ_c are time constants for the actor and critic traces respectively.
 272 Correspondingly, actor and critic trace vectors are denoted as \vec{c}_{ai} and \vec{c}_c . Note
 273 that \vec{c}_{ai} relates to the action neuron i and c_{aij} is set to one when an action neuron
 274 i and hidden neuron j fire at the same discrete time step.

275 Finally, after an action is selected, the environment provides the next obser-
 276 vation $\vec{x}(t+1)$ and reward signal $r(t+1)$. Based on this feedback, the temporal
 277 difference (TD) error is calculated as follows (Sutton & Barto, 2018):

$$\delta = r(t+1) + \gamma V(t+1) - V(t), \quad (9)$$

278 where $V(t)$ is the value of the hidden state at time t and γ is a discount parameter.
 279 Based on the TD error, value and action weights are updated:

$$\vec{w}_v(t+1) = \vec{w}_v(t) + \vec{c}_c(t) * \eta_c * \delta, \quad (10)$$

$$\vec{w}_{ai}(t+1) = \vec{w}_{ai}(t) + \vec{c}_{ai}(t) * \eta_a * \delta, \quad (11)$$

280 where \vec{w}_v is a vector of values, \vec{w}_{ai} are weights arriving at the action neuron i .
 281 Constants η_c and η_a are update rates for the critic and actor respectively. Finally,
 282 weights and thresholds of clustering layers are also modulated by the TD error:

$$\theta_i(t+1) = \theta_i(t) + \eta_{td} * \Delta\theta_i * |\delta| * c_i(t), \quad (12)$$

$$\vec{w}_i(t+1) = \vec{w}_i(t) + \eta_{td} * \Delta\vec{w}_i * |\delta| * c_i(t), \quad (13)$$

283 where η_{td} is the update rate and $c_i(t)$ is the activation trace of the postsynaptic
 284 neuron i . Following Equation 8, this trace is set to one each time neuron i pro-
 285 duces a spike and decays exponentially with time constant τ_i . This update occurs
 286 concurrently with unsupervised clustering described by Equations 4 and 5.

287 With the above update rule lower absolute TD error causes the neuron to
 288 follow the unsupervised clustering rule from Equations 4 and 5 and illustrated
 289 in Figure 2. Conversely, a higher positive or negative TD error signal makes the
 290 model more likely to retain the recent feature representation.

291 An overview of the proposed network is illustrated in Figure 6. In this ex-
 292 ample, the first clustering layer is divided into groups of three neurons, each
 293 with a WTA activation. The activation trace from this first layer is a higher di-
 294 mensional vector than the input. Both the first and second layers implement
 295 the FEAST clustering rule proposed by Afshar et al. (2020), as well as additional
 296 modulation by TD error, described by Equations 12 and 13.

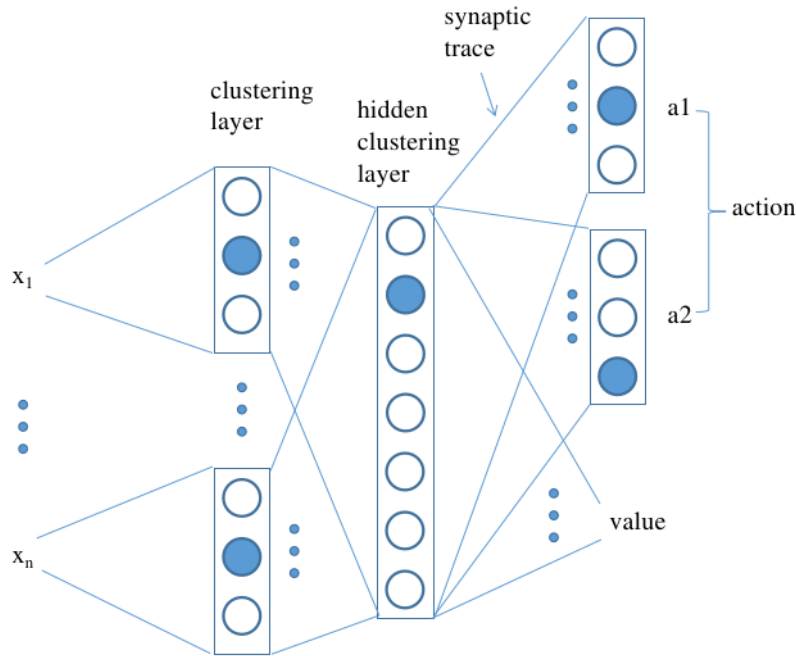
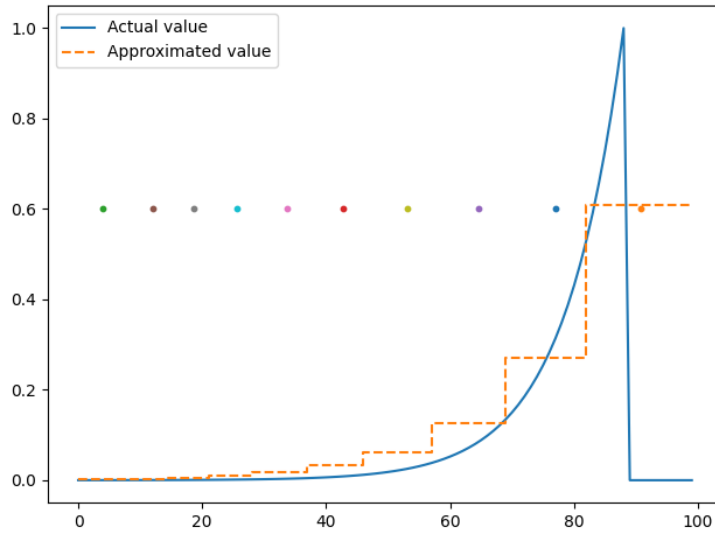


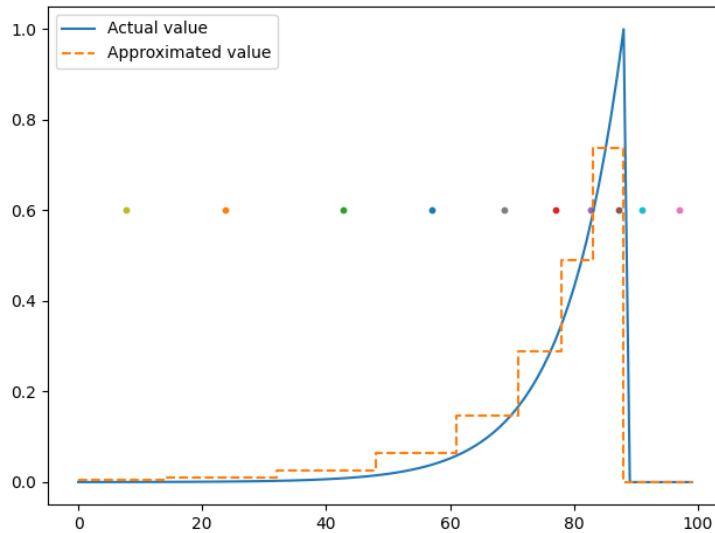
Figure 6: An overview of the presented network. In this example, each input scalar x_i is connected to a group of three neurons in the first clustering layer. A WTA activation is applied independently on each group and a resulting multi-hot vector is processed further by the hidden clustering layer. Another WTA activation function, this time applied to the entire layer, results in a single active neuron which represents a distinct hidden state. Orthogonal actions are independently encoded by subsequent groups of neurons and the value corresponding to the hidden state is computed based on sum of the synaptic weights. Eligibility traces are attached to both neurons and synapses for weight and threshold modulation.

297 A linear track experiment is used to illustrate the role of TD-modulated clus-
 298 tering. In this environment, the agent travels through a fixed track from position
 299 1 to 100 and each time-step moves the agent to the right by one unit. A single
 300 reward of +1 is provided at position 90 and once the end of the track is reached,
 301 the agent restarts at position 1. Considering a discount $\gamma = 0.9$, the value corre-
 302 sponding to each position is represented by a solid blue line in Figure 7. Since in
 303 the proposed architecture the state values are estimated from a hidden layer, a
 304 discrete approximation of a real-valued curve is formed by the ten hidden neu-

305 rons. This approximation is represented by a dotted orange line and the solid
306 dots correspond to the weights of these hidden neurons after 500 episodes. Note
307 that if no TD-modulation is used, the weights would converge to a uniform rep-
308 resentation of the observed state-space, as depicted in Figure 7a. On the other
309 hand, by adding modulation through TD-error, the weights will be skewed to-
310 wards the states that produce the highest TD-error, which is illustrated by a more
311 accurate approximation of the value curve in Figure 7b.



(a)



(b)

Figure 7: An illustration of the role of TD-modulated clustering for a more accurate value representation. Position of the colored dots on the X-axis represent the weights of the ten neurons used in the experiment. Thresholds are omitted for legibility.

312 4. Experimental evaluation

313 The proposed network is experimentally compared to a classical tabular actor-
314 critic algorithm with eligibility traces (TAC), as well as a state-of-the-art deep
315 reinforcement learning (DRL) algorithm PPO. Three classic control RL environ-
316 ments from OpenAI Gym (Brockman et al., 2016) are used for this evaluation:
317 mountain car, cart-pole and acrobot. The sections below provide a more detailed
318 description of these environments and baseline algorithms.

319 4.1. RL environments

320 4.1.1. Mountain car

321 The Mountain car is a classic RL control problem, illustrated in Figure 8. The
322 environment consists of a car that is stuck in a valley between two hills. The car
323 has limited power and is unable to climb the hills directly. The goal of the agent
324 is to learn how to control the car so that it can reach the top of the hill on the
325 right.

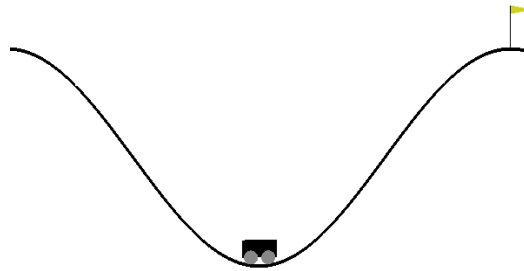


Figure 8: The mountain car environment (Brockman et al., 2016).

326 This environment has a two-dimensional state space, consisting of the posi-
327 tion and velocity of the car. The position is a continuous value that ranges from
328 -1.2 to 0.6, while the velocity ranges from -0.07 to 0.07. The action space is dis-
329 crete, consisting of three possible actions: push the car to the left, push the car
330 to the right, or do nothing.

331 The reward function in the Mountain car environment is designed to encour-
332 age the agent to reach the top of the hill on the right. The agent receives a reward
333 of -1 at each time step until it reaches the goal. This penalization is added to en-
334 courage the agent to reach the goal as quickly as possible. Once the agent reaches
335 the goal, the episode ends and the agent receives a reward of 0.

336 This is a non-trivial problem because of the long-term dependencies involved.
337 The agent must learn to build up momentum by moving back and forth in the
338 valley before it can climb the hill on the right. This requires the agent to balance
339 short-term rewards with long-term goals. Importantly, the goal state is extremely
340 unlikely to be reached by chance, i.e. random exploration, within the time limit
341 of 200 steps.

342 4.1.2. *Cart-pole*

343 The cart-pole environment in OpenAI Gym (Brockman et al., 2016) is another
344 classic RL problem, illustrated in Figure 9. The environment consists of a cart and
345 a pole that is attached to the cart by a free-moving joint. The goal of the agent
346 is to balance the pole on top of the cart for as long as possible.

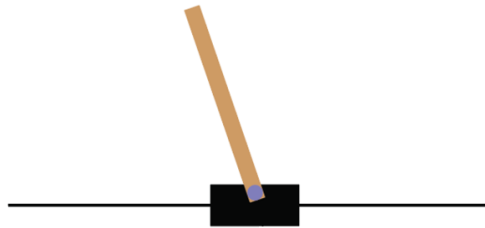


Figure 9: The Cart-pole environment (Brockman et al., 2016).

347 The state space of the Cart-pole environment is four-dimensional, consist-
348 ing of the position and velocity of the cart, and the angle and angular velocity
349 of the pole. The cart position and pole angle are continuous values, as well as
350 the respective velocities. The action space is discrete, consisting of two possible
351 actions: move the cart to the left or move the cart to the right.

352 The reward function in the Cart-pole environment is designed to encourage
353 the agent to balance the pole on top of the cart for as long as possible, limited
354 to 500 steps. The agent receives a reward of +1 at each time step while the pole
355 remains upright. The episode ends when the pole falls over or when the cart
356 moves too far to the left or right. Once the episode ends, the agent receives a
357 reward of 0.

358 The Cart-pole is a challenging RL problem because of its instability. The
359 agent must learn to balance the pole while also avoiding moving the cart too far
360 to either side.

361 *4.1.3. Acrobot*

362 The setup is illustrated in Figure 10 and the goal is to lift the tip of the robot to
363 a target level. The environment provides a six-dimensional observation consist-
364 ing of the sine and cosine of both joint angles, as well as the respective angular
365 velocities. The second joint is weakly actuated and the system includes gravita-
366 tional pull. To solve this task, the agent has to consistently swing the actuated
367 joint, building up the energy.

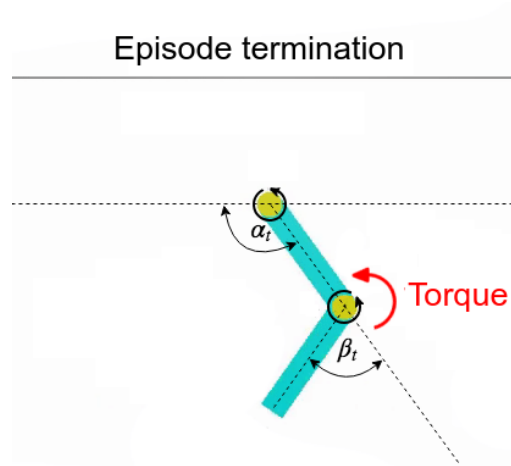


Figure 10: The acrobot environment (Brockman et al., 2016).

368 The reward function in the Acrobot environment is designed to encourage
369 the agent to swing the pendulum up to a vertical position. The agent receives a
370 reward of -1 at each time step, as with the other environments, this encourages
371 the agent to reach the goal as quickly as possible. When the pendulum reaches
372 the goal position the episode ends and the environment provides a reward of 0.

373 *4.2. Baseline algorithms*

374 *4.2.1. TAC*

375 The tabular actor-critic algorithm is based on a classical TD(λ) reinforcement
376 learning algorithm used to estimate the optimal value function of an MDP, given
377 a set of states, actions, and rewards (Sutton, 1988). It is a variant of the TD-
378 learning algorithm that incorporates eligibility traces, which allow for the accu-
379 mulation of TD-errors over multiple time steps.

380 At each time step, the algorithm updates the value function estimate of the
381 current state s using the TD-error δ , defined in Equation 9. This update is weighted

382 by the eligibility trace, which is a measure of the importance of the state s in the
383 current episode.

384 The eligibility traces of the actor and critic tables are updated at each time
385 step using the decay parameters τ_a and τ_c , as well as the discount factor γ . This
386 allows the algorithm to incorporate information from previous time steps into
387 the current update and improve the accuracy of the value function estimate.

388 The algorithm repeats this process for a fixed number of episodes, updating
389 the value function estimate and eligibility traces at each time step. The epsilon-
390 greedy exploration strategy is used to balance exploration and exploitation.

391 4.2.2. PPO

392 Proposed by Schulman et al. (2017), Proximal Policy Optimization (PPO) is
393 a RL algorithm used for training policy-based models, which directly optimizes
394 the policy function that maps states to actions. It is a variant of policy gradient
395 methods, which aim to maximize the expected reward of an agent by adjusting
396 the parameters of the policy function.

397 PPO uses a surrogate objective function that constrains the change in the
398 policy parameters to be small so that the agent does not deviate too far from
399 the previous policy. This makes the training process less brittle and prevents the
400 agent from making drastic policy changes. The PPO algorithm uses a clipping
401 technique to enforce this constraint on the policy updates. At each iteration, the
402 algorithm computes the ratio between the new and old policy probabilities for the
403 observed state-action pairs and uses this ratio to compute a surrogate objective
404 function. The surrogate objective function is then optimized using a gradient
405 descent algorithm, subject to a constraint that limits the size of the policy update.

406 The size of the policy update is controlled by a hyperparameter ϵ_{clip} , which
407 represents the maximum amount that the policy parameters can change in a
408 single update. If the ratio of the new and old policy probabilities exceeds $1 + \epsilon_{\text{clip}}$,
409 then the update is clipped to a maximum value of $1 + \epsilon_{\text{clip}}$. Similarly, if the ratio
410 is less than $1 - \epsilon_{\text{clip}}$, then the update is clipped to a minimum value of $1 - \epsilon_{\text{clip}}$.
411 This helps to prevent the policy from changing too much and ensures that the
412 updates are consistent with the previous policy.

413 Analogously to the actor-critic model in the proposed network, PPO also uses
414 a value function to estimate the expected reward of each state.

415 4.3. Hyperparameters

416 This section presents the main hyperparameters that were found to have an
417 impact on each algorithm’s performance during exploratory trials. A widely used

418 optimization framework *Optuna* (Akiba et al., 2019) is employed to iteratively
 419 search for a good set of hyperparameters for the proposed network and both of
 420 the baseline algorithms. More specifically, the Tree of Parzen estimators (TPE)
 421 Bergstra et al., 2011 algorithm is used for sequential optimization. After an initial
 422 random exploration for 10 trials, TPE aims at choosing a set of parameters that
 423 maximize an objective function. If a model with the same set of parameters is
 424 evaluated more than once, the final score is an average of all the trials within this
 425 set.

426 4.3.1. TAC

427 The tabular actor-critic baseline is optimized for 500 trials on each of the
 428 three benchmark problems: mountain car, cart-pole and acrobot. Each trial is
 429 composed of 1000 epochs and the optimizer aims at achieving the best average
 430 latency at the last 500 epochs. The best-performing parameters for each of these
 431 environments are indicated in Table 1 with letters **a**, **b** and **c** corresponding to
 432 mountain car, cart-pole and acrobot, respectively.

Table 1: Hyperparameter search space for the TAC baseline. Letters indicate the selected configuration for each environment: mountain car (**a**), cart-pole (**b**) and acrobot (**c**).

Hyperparameter	Search space
# of bins per dimension	[5, 10(b,c), 20(a)]
ϵ_{min}	[0.01(a), 0.05(b,c), 0.1]
ϵ decay time (# of episodes)	[100, 200(b,c), 500(a)]
Discount factor	[0.9(c), 0.95(a,b), 0.99]
Actor learning rate	[10^{-3} , 10^{-2} (b,c), 10^{-1} (a)]
Critic learning rate	[10^{-3} , 10^{-2} (b,c), 10^{-1} (a)]
τ_a	[1(a,b,c), 10, 20]
τ_c	[1, 10, 20(a,b,c)]

433 4.3.2. PPO

434 Table 2 presents the list of hyperparameters for the PPO algorithm, described
 435 in Section 4.2.2. The optimization process is identical to the TAC algorithm. Due

436 to the sparse rewards of the mountain car problem, the PPO algorithm was not
 437 used on this environment.

Table 2: Hyperparameter search space for the PPO baseline. Letters indicate the selected configuration for each environment: mountain car (**a**), cart-pole (**b**) and acrobot (**c**).

Hyperparameter	Search space
# of neurons in each hidden layer	[64(b,c), 128, 256]
# of hidden layers	[1(b), 2(c), 3]
Buffer size	[1k, 2k(b,c), 4k]
Learning rate	[10^{-3} , 10^{-4} (b,c), 10^{-5}]
Batch size	[32, 64(b,c), 128]
Discount factor	[0.9(c), 0.95, 0.99(b)]
# of surrogate loss optimization epochs	[5, 10(b,c), 20]
Clipping parameter ϵ_{clip}	[0.1, 0.2(b,c), 0.4]

438 4.3.3. Proposed model

439 The proposed model shares hyperparameters with the TAC algorithm, as the
 440 Actor-Critic part of the network is a neuromorphic implementation of this algo-
 441 rithm. However, a different search space is selected because the proposed Actor-
 442 Critic model does not evaluate the entire state-space of a given environment.
 443 Rather, a hidden layer of the clustering network is used to partition the state-
 444 space into a more compact and discrete representation.

445 In contrast to the baseline algorithms above, and due to the large number of
 446 adjustable parameters in the proposed model, a hybrid optimization strategy was
 447 adopted. The TPE algorithm was used alternatively with manual tuning, typi-
 448 cally adjusting a few parameters at a time. The final set of optimized parameters
 449 is presented in Table 3, with letters **a**, **b** and **c** indicating the hyperparameters
 450 found for mountain cat, cart-pole and acrobot environments. Note that only the
 451 acrobot environment benefited from a second clustering layer. Thus, an addi-
 452 tional optimized configuration with a single clustering layer is indicated by **d**.
 453 This configuration is used to evaluate the impact of the second clustering layer,
 454 as described in Section 4.5.

Table 3: Hyperparameter search space for the proposed network. Letters indicate the selected configuration for each environment: mountain car (**a**), cart-pole (**b**) and acrobot (**c** and **d**).

Hyperparameter	Search space
η	$[10^{-5}(\mathbf{a}), 10^{-4}, 10^{-3}(\mathbf{b}, \mathbf{c}, \mathbf{d}), 10^{-2}]$
η decay factor	$[10^{-3}(\mathbf{b}), 10^{-2}(\mathbf{d}), 10^{-1}(\mathbf{a}, \mathbf{c}), 1]$
η decay time (# of episodes)	$[100(\mathbf{b}, \mathbf{d}), 500(\mathbf{c}), 1000(\mathbf{a})]$
θ_{open}	$[10^{-3}(\mathbf{b}), 10^{-2}(\mathbf{a}, \mathbf{c}), 10^{-1}(\mathbf{d})]$
θ_{open} decay factor	$[10^{-3}(\mathbf{b}), 10^{-2}, 10^{-1}(\mathbf{a}, \mathbf{c}, \mathbf{d}), 1]$
θ_{open} decay time (# of episodes)	$[100(\mathbf{b}, \mathbf{d}), 500, 1000(\mathbf{a}, \mathbf{c})]$
# of neurons in the first clustering layer	$[10, 20(\mathbf{c}), 50, 100(\mathbf{a}, \mathbf{b}, \mathbf{d})]$
# of neurons in the second clustering layer	$[10, 20(\mathbf{c}), 50]$
η_{td}	$[10^{-3}(\mathbf{a}), 10^{-2}(\mathbf{c}, \mathbf{d}), 10^{-1}(\mathbf{b})]$
ϵ_{min}	$[0.01(\mathbf{a}, \mathbf{b}, \mathbf{c}, \mathbf{d}), 0.05, 0.1]$
ϵ decay time (# of episodes)	$[100, 200, 500(\mathbf{a}, \mathbf{b}, \mathbf{c}, \mathbf{d})]$
Discount factor	$[0.9, 0.95(\mathbf{b}, \mathbf{c}), 0.99(\mathbf{a}, \mathbf{d})]$
Actor learning rate	$[10^{-3}, 10^{-2}, 10^{-1}(\mathbf{a}, \mathbf{b}, \mathbf{c}, \mathbf{d})]$
Critic learning rate	$[10^{-3}, 10^{-2}(\mathbf{c}), 10^{-1}(\mathbf{a}, \mathbf{b}, \mathbf{d})]$
τ_a	$[1, 5(\mathbf{a}), 10(\mathbf{c}, \mathbf{d}), 20, 50(\mathbf{b})]$
τ_c	$[1, 5(\mathbf{a}), 10(\mathbf{b}, \mathbf{c}, \mathbf{d}), 20, 50]$

4.4. Results

The following experimental results are obtained from ten independent runs for each combination of an RL algorithm and a benchmark environment. A random agent ($\epsilon = 0$) is also included in the experiments. The results are presented as the average of the ten trials, with respect to each episode. Additionally, the trial with the best latency is shown separately as a dotted line and the shaded region indicates standard deviation, also relative to the episode.

462 4.4.1. Mountain car

463 The Mountain car environment has two input dimensions and a sparse re-
 464 ward. The PPO algorithm did not obtain good results on this benchmark unless
 465 the reward signal is modified to include a continuous reward related to proximity
 466 to the goal state. Because of this, the PPO algorithm is not included in the results
 467 presented in Figure 11. Also due to the sparse reward, a random agent is unable
 468 to terminate the episode before the time-out of 200 steps.

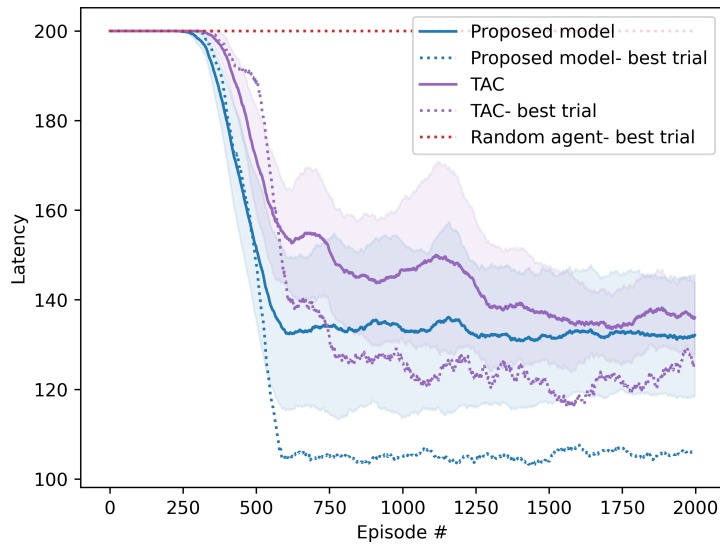


Figure 11: Average latency results on the Mountain car environment. Dotted lines correspond to the best out of ten trials and the shaded regions represent the standard deviation.

469 The proposed model and the TAC baseline present similar final latency values
 470 and learning speed on average. However, a comparison of the best trials (dotted
 471 lines) suggests that the proposed network can surpass the tabular algorithm. It
 472 is also worth noting that the observation space of the actor-critic TAC in this
 473 environment consists of the entire state space, discretized using 20 bins, giving
 474 a total of 400 discrete states. Meanwhile, the proposed network employs 100
 475 neurons for clustering the real-valued 2D input from the environment, resulting
 476 in 100 discrete states for the subsequent actor-critic component. This reduction
 477 in the state-space becomes more significant in the next benchmark environments

478 with higher state dimensions. It can also contribute to the faster learning rate
479 observed when comparing both average and best latency curves.

480 4.4.2. *Cart-pole*

481 The proposed model is also compared to baselines on the Cart-pole environ-
482 ment, as illustrated in Figure 12. Differently from the Mountain car problem, the
483 reward is not sparse and is proportional to the time the agent is able to keep the
484 pole in balance. While all three of the evaluated models are able to significantly
485 improve the balancing time after 250 epochs, PPO provides the most stable control
486 over the ten independent runs. The proposed model obtains a comparable
487 performance to PPO on the best run and, as in the previous experiment, is better
488 than TAC in terms of both average and the best runs.

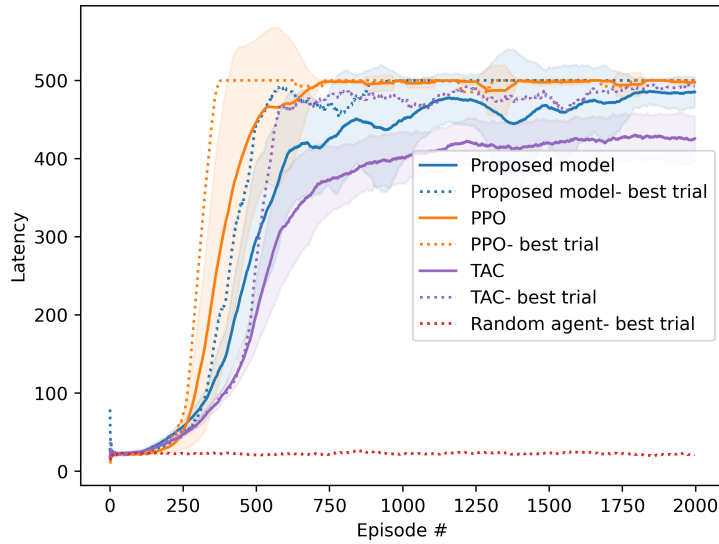


Figure 12: Average latency results on the Cart-pole environment. Dotted lines correspond to the best out of ten trials and the shaded regions represent the standard deviation.

489 As described in Section 4.3.3, the proposed network uses a single clustering
490 layer with 100 neurons, providing a reduced discrete state space for the actor-
491 critic network. On the other hand, the TAC algorithm uses 10 bins for each input
492 dimension, giving a total of 10^4 discrete states. While increasing the number of

493 bins can result in improved performance over time, this has the drawback of
 494 slower learning speed. Thus, the proposed clustering layer is able to provide
 495 enough resolution in the state-space for solving the Cart-pole without requiring
 496 a very large number of neurons.

497 4.4.3. Acrobot

498 The Acrobot environment combines a sparse reward with additional input di-
 499 mensions, making it the most challenging of the three considered benchmarks.
 500 On this task, the proposed network is able to achieve significantly better perfor-
 501 mance by using two clustering layers. The first layer contains 20 neurons per
 502 dimension, or a total of 120 neurons, with 6 active at any given time-step. The
 503 second layer reduces this state-space to just 20 neurons in total, a substantial
 504 reduction compared to 10^6 states observed by the TAC algorithm.

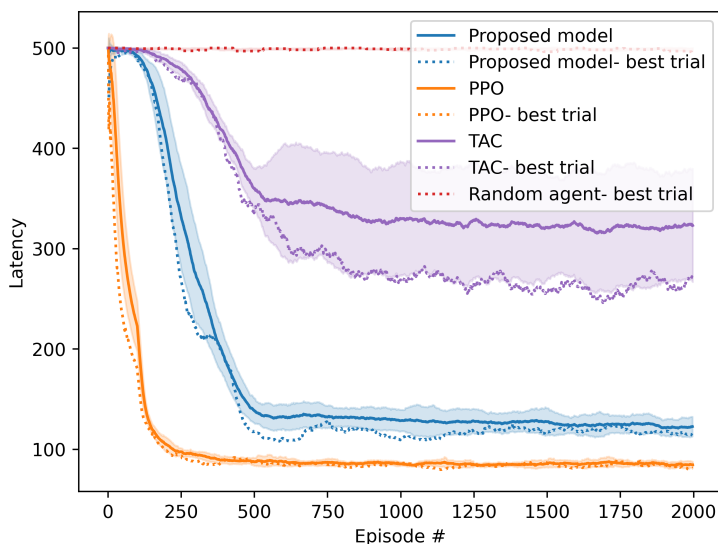


Figure 13: Average latency results on the Acrobot environment. Dotted lines correspond to the best out of ten trials and the shaded regions represent the standard deviation.

505 While the PPO algorithm is significantly better than the proposed one in
 506 terms of learning speed and control precision, the proposed model is still able to
 507 find a stable control strategy for the Acrobot problem.

508 *4.5. Discussion and summary*

509 An obvious advantage of the proposed network over a tabular RL algorithm is
 510 that the state space observed by the actor is drastically reduced. Table 4 provides
 511 a comparison of the proposed model and the Tabular Actor-Critic (TAC) in terms
 512 of state space requirements. The difference becomes more significant when the
 513 number of input dimensions is increased.

Table 4: Comparison between the proposed model and the Tabular Actor-Critic (TAC) in terms of state space requirements

Environment	Algorithm	State space
Mountain car	Proposed	1×10^2
	TAC	4×10^2
Cart-pole	Proposed	1×10^2
	TAC	1×10^4
Acrobot	Proposed	2×10^1
	TAC	1×10^6

514 We consider the Cart-pole and Acrobot environments for an additional abla-
 515 tion study with the aim to evaluate the impact on the performance of the individ-
 516 ual components of the proposed network. In order to provide a more statistically
 517 significant set of results, each experiment consists of 30 independent runs using
 518 a specific configuration of the algorithm. Average latency and standard deviation
 519 are evaluated using an unpaired t-test with 95% significance.

520 The proposed network has two synaptic plasticity models for the clustering
 521 layers: passive clustering that drives neurons to evenly represent the observed
 522 state-space and TD-error modulation that encourages a denser distribution near
 523 states with higher absolute TD-error (see Section 3.2 for more details). Each of
 524 these components is individually disabled from the proposed model and evalu-
 525 ated on the cart-pole environment. The average latency and standard deviation
 526 are calculated from the last 1000 episodes of each run, once a more stable con-
 527 trol is reached. A qualitative comparison is presented in Figure 14, while the
 528 statistical significance analysis is based on corresponding data from Table 5.

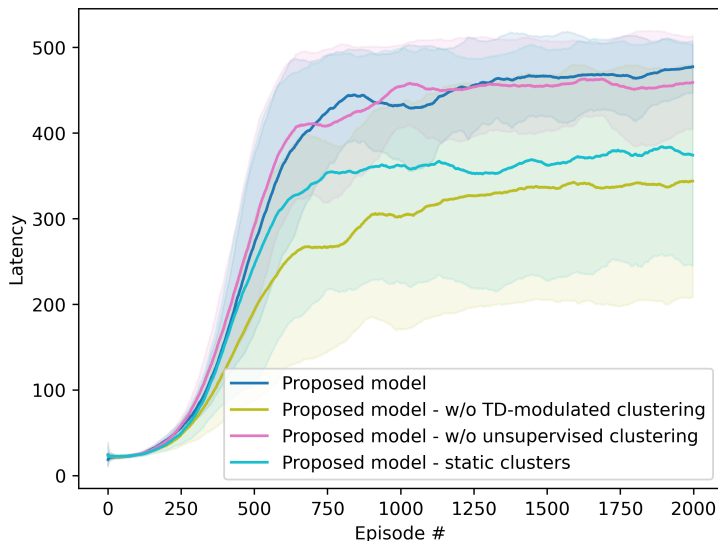
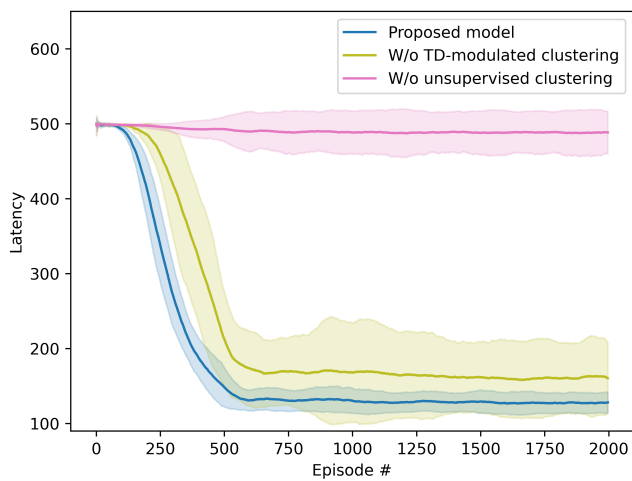


Figure 14: An ablation study of the proposed model on the cart-pole environment. The shaded regions represent the standard deviation.

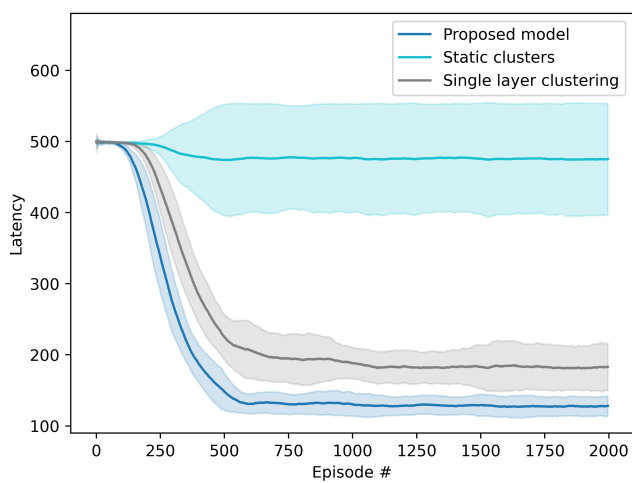
529 The comparison of average latencies in Table 5 suggests that TD-error modulation
 530 plays a significant role in the performance of the network. Meanwhile,
 531 there is no statistically significant difference between a configuration with and
 532 without passive clustering enabled on the cart-pole environment. Interestingly,
 533 both plasticity rules are found to be significant in the next ablation study on the
 534 acrobot environment.

535 A similar ablation study on the acrobot environment is presented in Figure
 536 15 and Table 6. However, since the proposed network for this environment has
 537 a second clustering layer, another configuration is optimized with a single clustering
 538 layer in order to evaluate the impact of this feature. Simply removing
 539 a layer from the proposed configuration would not result in a fair comparison,
 540 since the other hyperparameters also have to be adjusted to better fit the new
 541 configuration. Thus, an additional optimization run with 500 trials is performed,
 542 considering the same range of hyperparameters presented in Table 3.

543 Overall, each of the considered changes to the proposed architecture results
 544 in a statistically significant drop in performance, when compared to the initial
 545 configuration. In contrast to the previous experiment with the cart-pole envi-



(a)



(b)

Figure 15: An ablation study of the proposed model on the acrobot environment. The shaded regions represent the standard deviation.

Table 5: Average and standard deviation of the latency curve for the ablation study on the cart-pole environment. The shaded regions represent the standard deviation.

Configuration	Average latency (std)	Significant change?
Proposed	460 (52)	
W/o TD-modulated clustering	332 (134)	✓
W/o unsupervised clustering	456 (56)	
Static clusters	367 (132)	✓

546 ronment, the unsupervised clustering plays a more significant role than the TD-
 547 modulated one.

Table 6: Average and standard deviation of the latency curve for the ablation study on the acrobot environment

Configuration	Average latency (std)	Significant change?
Proposed	128 (14)	
Static clusters	475 (78)	✓
Single clustering layer	183 (29)	✓
W/o TD-modulated clustering	163 (54)	✓
W/o unsupervised clustering	488 (29)	✓

548 Finally, the proposed neuromorphic approach is fundamentally different from
 549 traditional deep reinforcement learning (DRL) models in term of both memory
 550 usage and the amount of synaptic updates that are applied to the network dur-
 551 ing learning. Firstly, while PPO and similar DRL algorithms use a large mem-
 552 ory buffer for storing previous transitions in the environment, the current ap-
 553 proach relies on synaptic traces. Secondly, the backpropagation algorithm re-
 554 quires global information about the network, while in the proposed model only
 555 local computations are applied for synaptic plasticity. Thirdly, during training
 556 the synapses of the actor-critic network used by PPO are modified several times

557 over a batch of data retrieved from the memory buffer. On the other hand, the
558 synaptic updates on the proposed model are performed once at each time-step
559 by using a broadcasted TD-error signal and eligibility traces.

560 **5. Conclusion and final remarks**

561 This work provides a novel neuromorphic architecture aimed at solving rein-
562 forcement learning problems with real-valued observations. The proposed net-
563 work contains clustering layers, based on earlier work by Afshar et al., 2020 and
564 Bethi et al., 2022, with an introduction of TD-error modulation and eligibility
565 traces. The impact of the main components introduced in this architecture is
566 evaluated in an ablation study and shown to have a significant impact on perfor-
567 mance.

568 The network’s effectiveness is assessed against a tabular actor-critic algo-
569 rithm with eligibility traces, as well as a state-of-the-art deep learning model,
570 Proximal Policy Optimization (PPO). The proposed model outperforms the tabu-
571 lar algorithm in terms of learning speed and accuracy consistently, demonstrat-
572 ing its capability to discover stable control policies for three control problems
573 involving 2, 4 and 6 input dimensions.

574 While it does not surpass the PPO-based controller in terms of optimal per-
575 formance, our network offers an appealing trade-off in terms of memory and
576 hardware implementation requirements. This is because the proposed model
577 does not require an external memory buffer and the synaptic plasticity occurs
578 online, driven solely by local learning rules and a broadcasted TD-error signal.
579 These aspects provide a more biologically plausible learning model, which in fu-
580 ture may lead to more efficient algorithms in terms of computational and memory
581 requirements.

582 *5.1. Future work*

583 Future research can focus on the following directions:

- 584 • Automatic parameter and architecture tuning – the experiments suggest
585 that the model’s performance is sensitive to the choice of several param-
586 eters. Future work could discover how to best apply evolutionary algo-
587 rithms to the problem of finding architecture and parameter set for a given
588 problem.
- 589 • Scalability to more complex problems – the proposed model was effective
590 in solving control problems with 2, 4, and 6 input dimensions. Future work

591 could investigate the model’s scalability to problems with even larger in-
592 put dimensions. A hierarchic organization in the clustering layers is one
593 possible strategy for learning from an increased number of dimensions.

- 594 • Hardware implementation – the study highlighted the potential hardware
595 efficiency of the proposed model. Future work could focus on the actual
596 implementation of this architecture in hardware, and investigate its per-
597 formance in real-world applications.
- 598 • Population coding – the current method does not rely on population cod-
599 ing, which can increase the number of parameters within the network and
600 lead to slower learning speeds. However, more robust learning and bet-
601 ter scalability are potential benefits of this encoding method (Tang et al.,
602 [2021](#)). Future work could explore a hybrid approach that combines the cur-
603 rent method with elements of population coding, to potentially improve
604 performance without significantly increasing the number of parameters.

605 **Acknowledgment**

606 The authors would like to thank FACEPE, CNPq and CAPES (Brazilian Re-
607 search Agencies) for their financial support.

608 **References**

- 609 Afshar, S., Ralph, N., Xu, Y., Tapson, J., Schaik, A. v., & Cohen, G. (2020). Event-
610 based feature extraction using adaptive selection thresholds. *Sensors*, *20*(6),
611 1600.
- 612 Akiba, T., Sano, S., Yanase, T., Ohta, T., & Koyama, M. (2019). Optuna: A next-
613 generation hyperparameter optimization framework. *Proceedings of the*
614 *25rd ACM SIGKDD International Conference on Knowledge Discovery and*
615 *Data Mining*.
- 616 Akl, M., Ergene, D., Walter, F., & Knoll, A. (2023). Toward robust and scalable
617 deep spiking reinforcement learning. *Frontiers in Neurorobotics*, *16*, 314.
- 618 Ballard, D. H., & Jehee, J. (2012). Dynamic coding of signed quantities in cortical
619 feedback circuits. *Frontiers in psychology*, *3*, 254.
- 620 Bellec, G., Scherr, F., Subramoney, A., Hajek, E., Salaj, D., Legenstein, R., & Maass,
621 W. (2020). A solution to the learning dilemma for recurrent networks of
622 spiking neurons. *Nature communications*, *11*(1), 1–15.

- 623 Bergstra, J., Bardenet, R., Bengio, Y., & Kégl, B. (2011). Algorithms for hyper-
624 parameter optimization. *Advances in neural information processing systems*, 24.
625
- 626 Bethi, Y., Xu, Y., Cohen, G., Van Schaik, A., & Afshar, S. (2022). An optimized
627 deep spiking neural network architecture without gradients. *IEEE Access*,
628 10, 97912–97929.
- 629 Brockman, G., Cheung, V., Pettersson, L., Schneider, J., Schulman, J., Tang, J., &
630 Zaremba, W. (2016). Openai gym. *arXiv preprint arXiv:1606.01540*.
- 631 Chevtchenko, S. F., & Ludermir, T. B. (2020). Learning from sparse and delayed re-
632 wards with a multilayer spiking neural network. *2020 International Joint
633 Conference on Neural Networks (IJCNN)*, 1–8.
- 634 Diehl, P. U., & Cook, M. (2015). Unsupervised learning of digit recognition us-
635 ing spike-timing-dependent plasticity. *Frontiers in computational neuro-
636 science*, 9, 99.
- 637 Florian, R. V. (2007). Reinforcement learning through modulation of spike-timing-
638 dependent synaptic plasticity. *Neural Computation*, 19(6), 1468–1502.
- 639 Frémaux, N., & Gerstner, W. (2016). Neuromodulated spike-timing-dependent
640 plasticity, and theory of three-factor learning rules. *Frontiers in neural
641 circuits*, 9, 85.
- 642 Frémaux, N., Sprekeler, H., & Gerstner, W. (2013). Reinforcement learning us-
643 ing a continuous time actor-critic framework with spiking neurons. *PLoS
644 computational biology*, 9(4), e1003024.
- 645 Friedrich, J., Urbanczik, R., & Senn, W. (2014). Code-specific learning rules im-
646 prove action selection by populations of spiking neurons. *International
647 journal of neural systems*, 24(05), 1450002.
- 648 Gallego, G., Delbrück, T., Orchard, G., Bartolozzi, C., Taba, B., Censi, A., Leuteneg-
649 ger, S., Davison, A. J., Conradt, J., Daniilidis, K., et al. (2020). Event-based
650 vision: A survey. *IEEE transactions on pattern analysis and machine intel-
651 ligence*, 44(1), 154–180.
- 652 Gerstner, W., Lehmann, M., Liakoni, V., Corneil, D., & Brea, J. (2018). Eligibility
653 traces and plasticity on behavioral time scales: Experimental support of
654 neohebbian three-factor learning rules. *Frontiers in neural circuits*, 12.
- 655 Haessig, G., Milde, M. B., Aceituno, P. V., Oubari, O., Knight, J. C., Van Schaik,
656 A., Benosman, R. B., & Indiveri, G. (2020). Event-based computation for
657 touch localization based on precise spike timing. *Frontiers in neuroscience*,
658 420.

- 659 Hwangbo, J., Lee, J., Dosovitskiy, A., Bellicoso, D., Tsounis, V., Koltun, V., & Hut-
660 ter, M. (2019). Learning agile and dynamic motor skills for legged robots.
661 *arXiv preprint arXiv:1901.08652*.
- 662 Izhikevich, E. M. (2007). Solving the distal reward problem through linkage of
663 stdp and dopamine signaling. *Cerebral cortex*, 17(10), 2443–2452.
- 664 Jitsev, J., Morrison, A., & Tittgemeyer, M. (2012). Learning from positive and
665 negative rewards in a spiking neural network model of basal ganglia. *The*
666 *2012 International Joint Conference on Neural Networks (IJCNN)*, 1–8.
- 667 Lagorce, X., Orchard, G., Galluppi, F., Shi, B. E., & Benosman, R. B. (2016). Hots:
668 A hierarchy of event-based time-surfaces for pattern recognition. *IEEE*
669 *transactions on pattern analysis and machine intelligence*, 39(7), 1346–1359.
- 670 Legenstein, R., Pecevski, D., & Maass, W. (2008). A learning theory for reward-
671 modulated spike-timing-dependent plasticity with application to biofeed-
672 back. *PLoS Comput Biol*, 4(10), e1000180.
- 673 Lichtsteiner, P., Posch, C., & Delbruck, T. (2008). A 128×128 120 dB 15μ s latency
674 asynchronous temporal contrast vision sensor. *IEEE Journal of Solid-State*
675 *Circuits*, 43(2), 566–576.
- 676 Lukoševičius, M., & Jaeger, H. (2009). Reservoir computing approaches to recur-
677 rent neural network training. *Computer science review*, 3(3), 127–149.
- 678 Maass, W., Natschläger, T., & Markram, H. (2002). Real-time computing without
679 stable states: A new framework for neural computation based on pertur-
680 bations. *Neural computation*, 14(11), 2531–2560.
- 681 Mnih, V., Kavukcuoglu, K., Silver, D., Rusu, A. A., Veness, J., Bellemare, M. G.,
682 Graves, A., Riedmiller, M., Fidjeland, A. K., Ostrovski, G., et al. (2015).
683 Human-level control through deep reinforcement learning. *Nature*, 518(7540),
684 529.
- 685 Neftci, E. O., Mostafa, H., & Zenke, F. (2019). Surrogate gradient learning in spik-
686 ing neural networks: Bringing the power of gradient-based optimization
687 to spiking neural networks. *IEEE Signal Processing Magazine*, 36(6), 51–63.
- 688 Orchard, G., Meyer, C., Etienne-Cummings, R., Posch, C., Thakor, N., & Benos-
689 man, R. (2015). Hfirst: A temporal approach to object recognition. *IEEE*
690 *transactions on pattern analysis and machine intelligence*, 37(10), 2028–
691 2040.
- 692 Posch, C., Matolin, D., & Wohlgenannt, R. (2010). A qvga 143 db dynamic range
693 frame-free pwm image sensor with lossless pixel-level video compression
694 and time-domain cds. *IEEE Journal of Solid-State Circuits*, 46(1), 259–275.

- 695 Potjans, W., Diesmann, M., & Morrison, A. (2011). An imperfect dopaminergic
696 error signal can drive temporal-difference learning. *PLoS computational*
697 *biology*, 7(5), e1001133.
- 698 Potjans, W., Morrison, A., & Diesmann, M. (2009). A spiking neural network
699 model of an actor-critic learning agent. *Neural computation*, 21(2), 301–
700 339.
- 701 Ralph, N., Joubert, D., Jolley, A., Afshar, S., Tothill, N., van Schaik, A., & Cohen,
702 G. (2022). Real-time event-based unsupervised feature consolidation and
703 tracking for space situational awareness. *Frontiers in neuroscience*, 16.
- 704 Schrauwen, B., Verstraeten, D., & Van Campenhout, J. (2007). An overview of
705 reservoir computing: Theory, applications and implementations. *Proceed-*
706 *ings of the 15th european symposium on artificial neural networks*. p. 471–
707 482 2007, 471–482.
- 708 Schulman, J., Wolski, F., Dhariwal, P., Radford, A., & Klimov, O. (2017). Proximal
709 policy optimization algorithms. *arXiv preprint arXiv:1707.06347*.
- 710 Schuman, C. D., Kulkarni, S. R., Parsa, M., Mitchell, J. P., Date, P., & Kay, B. (2022).
711 Opportunities for neuromorphic computing algorithms and applications.
712 *Nature Computational Science*, 2(1), 10–19.
- 713 Serre, T., Wolf, L., Bileschi, S., Riesenhuber, M., & Poggio, T. (2007). Robust ob-
714 ject recognition with cortex-like mechanisms. *IEEE transactions on pat-*
715 *tern analysis and machine intelligence*, 29(3), 411–426.
- 716 Sutton, R. S. (1988). Learning to predict by the methods of temporal differences.
717 *Machine learning*, 3(1), 9–44.
- 718 Sutton, R. S., & Barto, A. G. (2018). *Reinforcement learning: An introduction*. MIT
719 press.
- 720 Tang, G., Kumar, N., Yoo, R., & Michmizos, K. (2021). Deep reinforcement learn-
721 ing with population-coded spiking neural network for continuous con-
722 trol. *Conference on Robot Learning*, 2016–2029.
- 723 Vasilaki, E., Frémaux, N., Urbanczik, R., Senn, W., & Gerstner, W. (2009). Spike-
724 based reinforcement learning in continuous state and action space: When
725 policy gradient methods fail. *PLoS computational biology*, 5(12), e1000586.
- 726 Weidel, P., Duarte, R., & Morrison, A. (2021). Unsupervised learning and clustered
727 connectivity enhance reinforcement learning in spiking neural networks.
728 *Frontiers in computational neuroscience*, 15, 543872.
- 729 Xu, Y., Perera, S., Bethi, Y., Afshar, S., & van Schaik, A. (2022). Event-driven spec-
730 trotemporal feature extraction and classification using a silicon cochlea
731 model. <https://doi.org/10.48550/ARXIV.2212.07136>